Nano Research

Open Access

Research Article

# Defect engineering of zinc-based metal organic framework with enhanced ROS generation for antibacterial and wound healing applications

Wenwen Cheng[1,2,§], Wang Wang[1,§], Zhijun Zhou[1], Hang Yin[1], Ye Yang[2], Feng Xiao[3], Wenjie You[3], Zesheng Chen[1,2], Weikang Hu[2] ✉, Xingyuan Xiao[1] ✉, and Zijian Wang[1] ✉

[1] *Department of Urology, Hubei Key Laboratory of Urological Diseases, Zhongnan Hospital of Wuhan University, Wuhan 430071, China*
[2] *Hubei Province Key Laboratory of Biotechnology of Chinese Traditional Medicine, College of Health Science and Engineering, Hubei University, Wuhan 430062, China*
[3] *Orthopaedic Hospital, The First Affiliated Hospital, Jiangxi Medical College, Nanchang University, Nanchang 330006, China*
§ *Wenwen Cheng and Wang Wang contributed equally to this work.*

**Cite this article:** *Nano Research*, **2026**, *19*, 94908545. https://doi.org/10.26599/NR.2026.94908545

**ABSTRACT:** Bacterial infection in chronic skin defect poses a global healthcare challenge, fueled by antibiotic overuse and bacterial resistance. Zinc-based metal-organic frameworks (Zn-MOFs) with pro-oxidative nanozyme-like activity and broad-spectrum antibacterial activity, complemented by their inherent biocompatibility, have emerged as a promising alternative to antibiotics. However, the translational applications of Zn-MOFs are limited by suboptimal enzyme-mimicking catalytic activity, inadequate biodistribution and target site accumulation. To overcome these limitations, this study establishes a strategy of oxygen vacancy (Ov)-based defect engineering combined with microneedle-mediated transdermal delivery. An Ov-rich $Zn^{2+}/H_2BDC$ (Ov-ZBC) MOF is first synthesized by two-step reactions, and then immobilized into the tips of gelatin methacryloyl (GelMA) microneedles to obtain the double-layer GelMA/Ov-ZBC (GOZ) microneedles. Ov-ZBC MOFs demonstrate abundant Ov defects, which consequently led to a superior reactive oxygen species (ROS) production ability. Under visible light irradiation, GOZ microneedles inhibit bacterial survival and proliferation by producing ROS and releasing $Zn^{2+}$. Additionally, they accelerate the healing of *S. aureus*-infected wounds through multimodal mechanisms, such as anti-inflammatory, M2 macrophage polarization, and promoting cell proliferation. In conclusion, this study not only develops an antibiotic-free theranostic platform, but also provides a proof-of-concept for modifying Zn-MOFs, thereby paving the way for their advanced biomedical applications.

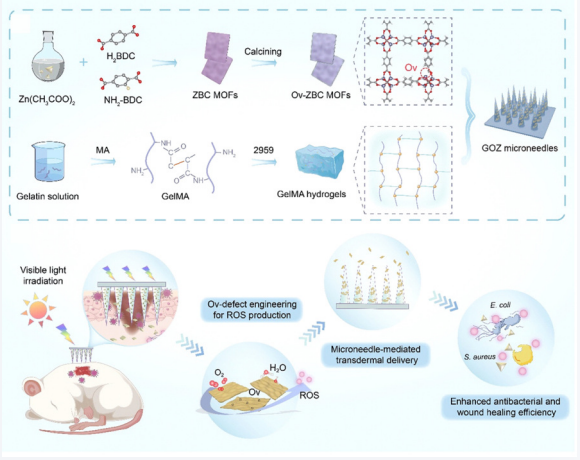


**KEYWORDS:** microneedle, wound healing, antibacterial, gelatin methacryloyl (GelMA), metal-organic framework (MOF), reactive oxygen species (ROS)

## 1 Introduction

Bacterial infection, primarily induced by *Staphylococcus* and *Streptococcus*, remains one of the major obstacles in the treatment of chronic skin wounds and defects, often resulting in delayed healing, excessive inflammation, and poor tissue regeneration [1]. While advanced antibiotic combinations are a powerful tool against bacterial infection, their use inevitably leads to side effects, including the development of bacterial resistance and the disruption of local immune homeostasis [2–4]. These challenges have driven increasing interest in antibiotic-free antibacterial strategies that can simultaneously eliminate bacteria and promote wound repair [5].

Nanozymes, a class of nanomaterial-based enzyme mimics, were

**Received:** December 13, 2025; **Revised:** February 5, 2026
**Accepted:** February 6, 2026

✉Address correspondence to Weikang Hu, Huwkang@hubu.edu.cn; Xingyuan Xiao, xiaoxingyuan@whu.edu.cn; Zijian Wang, Zijianwang@whu.edu.cn

first reported by Yan et al. in 2007 [6]. Pro-oxidative nanozymes have emerged as a promising alternative by catalyzing the generation of reactive oxygen species (ROS), which disrupt bacterial redox homeostasis and induce membrane damage [7, 8]. However, a key obstacle to the translational applications of nanozymes is their suboptimal catalytic activity for ROS generation *in vivo*, coupled with uncontrolled biodistribution and insufficient accumulation at target sites [9, 10].

Zinc-based metal organic framework (Zn-MOFs) are porous crystalline materials with a periodic network structure, which is formed through the self-assembly of zinc ions ($Zn^{2+}$) as metal centers and organic linkers via coordination bonds [11]. Nanozyme-like activities have been observed in Zn-MOFs, indicating their potential for biomimetic catalysis. Zn-MOFs have attracted particular attention due to their intrinsic biocompatibility and a unique "two-hit" antibacterial mechanism that combines ROS generation with $Zn^{2+}$ release [12]. In 2025, Ma et al. reported a $Zn^{2+}/H_2BDC$ (ZBC) MOF with superior antibacterial properties and lower cytotoxicity [13]. Despite these advantages, the clinical translation of Zn-MOF-based antibacterial systems remains limited. Inherent obstacles still exist in the translational applications of nanozymes. More importantly, most existing studies primarily focus on bactericidal performance, while the specific role of the nanozyme-like activity in the antibacterial mechanisms and guide tissue regeneration have not been explored. Given these limitations, tailored modifications to ZBC MOFs are necessary to enhance their efficacy.

Defect engineering emerges as an effective strategy to regulate the electronic structure and catalytic behavior of nanomaterials without altering their overall composition or framework [14–16]. In particular, oxygen vacancy (Ov) defects, featured by oxygen escaping from the lattice, can introduce localized electronic states, narrow band gaps, and promote interfacial charge transfer, thereby enhancing light absorption and ROS generation efficiency [17]. Although Ov defect has been widely applied to various pro-oxidative nanozymes, including those with peroxidase (POD), and superoxide dismutase (SOD)-like activities [18], its systematic implementation in MOF-based antimicrobial platforms—particularly the transition from mere catalytic activity enhancement to controlled delivery and targeted activation—remains to be further optimized.

Microneedle-based transdermal delivery systems provide a compelling solution to this challenge. Our group previously developed several kinds of biomolecular microneedles [19, 20]. They are composed of gelatin methacryloyl (GelMA) hydrogels as the polymer skeleton, and various nanoparticles as the cargoes. GelMA hydrogels absorb wound exudates, maintain a moist and clean microenvironment, provide vital physiochemical and biological cues for guiding cell regeneration [21, 22]. The sharp microneedle tips penetrate skin painlessly and deliver cargoes (nanoparticles) precisely to wound sites [23, 24]. In response to external stimuli like near-infrared (NIR) light, the nanoparticles produce ROS or other bioactive molecules for accelerating wound healing [25, 26]. As a theranostic platform, microneedles offer distinct advantages over conventional drug delivery systems. Based on previous research, it is assumed that the modified ZBC MOFs can be integrated with GelMA microneedles to improve their tissue target and biodistribution.

Herein, this study proposes a defect-driven, visible-light-activated antibacterial–immune–regenerative cascade based on oxygen-vacancy-enriched Zn-MOFs integrated into a GelMA microneedle system. A diagram of this study is shown in Scheme 1. Oxygen-vacancy-rich ZBC-MOFs (Ov-ZBC) were synthesized via a two-step hydrothermal–calcination strategy, endowing the material with enhanced visible-light absorption and burst ROS generation capability. The Ov-ZBC MOFs were subsequently immobilized into the tips of double-layer GelMA microneedles to achieve precise transdermal delivery and localized activation. Under visible light irradiation, the system triggers a synergistic antibacterial effect through ROS oxidation and $Zn^{2+}$ release, rapidly reducing bacterial burden. Beyond bacterial eradication, this antibacterial event initiates a favorable immune-regulatory cascade, characterized by inflammation attenuation, macrophage M2 polarization, and accelerated tissue regeneration. The results will demonstrate the potential of Ov-based defect engineering combined with microneedle-mediated transdermal delivery to effectively modify Zn-MOFs for biomedical applications. The products of this study will be extensively used for treating chronic skin defect and other wounds.

## 2 Results and discussion

### 2.1 Oxygen-vacancy engineering enhances ROS generation in Zn-MOFs

To elucidate how oxygen-vacancy engineering fundamentally alters the catalytic behavior of Zn-based MOFs, we first investigated the structural and electronic consequences induced by oxygen vacancy incorporation. The results of scanning electron microscope (SEM) observation are shown in Fig. 1(a). Both the ZBC and Ov-ZBC MOFs exhibited a comparable sheet-like structure at nanometer grade. As shown in Fig. 1(b), the oxygen vacancy-associated trapped electrons were characterized by electron paramagnetic resonance (EPR) test. From the EPR spectra, Ov-ZBC MOFs exhibited a strong signal peak at $g$ = 2.003, indicating the successful introduction of oxygen vacancy [27].

Furthermore, X-ray diffraction (XRD), Fourier transform infrared spectroscopy (FT-IR), and X-ray photoelectron spectroscopy (XPS) were employed to characterize the chemical structure and composite of ZBC and Ov-ZBC MOFs. Figure 1(c) shows the XRD patterns. The characteristic peaks of Ov-ZBC MOFs at $2\theta$ = 6.88°, 9.71°, 13.74°, and 15.35°, respectively corresponded to the (200), (220), (400), and (331) crystal planes, which are consistent with those of ZBC MOFs [28]. This phenomenon confirmed the preservation of crystalline structure after defect engineering, excluding phase transformation or structural collapse as contributing factors to the observed performance differences.

Figure 1(d) displays the FT-IR spectra. The broad peak at 3450 $cm^{-1}$ was attributed to the absorption of atmospheric water by the samples, representing the stretching vibration of O–H bonds or uncoordinated carboxyl OH groups [29]. Peaks at 1596 and 1382 $cm^{-1}$ were assigned to the asymmetric and symmetric vibrations of the carboxyl groups (–COOH) in terephthalic acid, respectively [30]. The peak at 1505 $cm^{-1}$ arose from the stretching vibration of C=C bonds in 1,4-benzenedicarboxylate (BDC). The peak at 535 $cm^{-1}$ corresponded to the stretching vibration of Zn–O bonds at the MOF centers, confirming successful coordination between zinc and the ligand [31].

The existence of oxygen vacancies in Ov-ZBC was further

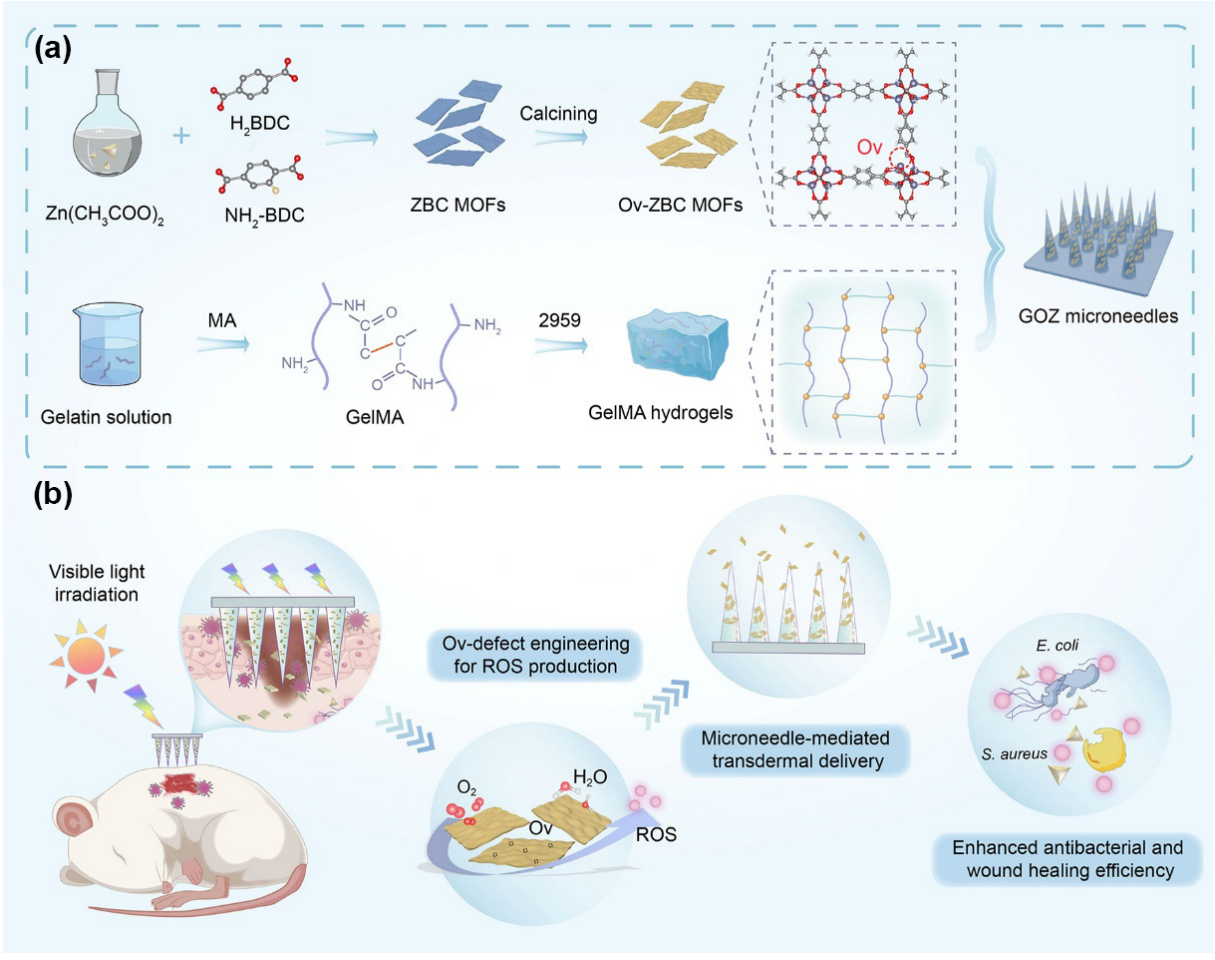


**Scheme 1** Zn-MOFs were modified for antibacterial and wound healing applications. (a) A diagram showing the preparation methods of Ov-ZBC MOFs and composite GOZ microneedles. (b) The microneedles accelerate *S. aureus*-infected wound healing. The role of Ov-based defect engineering and microneedle-mediated transdermal delivery was highlighted.

verified by the O 1s XPS spectrum shown in Fig. 1(e). Peaks at 531.48 and 532.08 eV corresponded to O–C=O and C=O species respectively, representing oxygen atoms from carboxylic acid groups in $H_2BDC$ and Zn–O bonds in the MOF framework [32]. The peak at 532.08 eV indicates the presence of oxygen vacancies [33]. Peak fitting analysis revealed that the oxygen vacancy content in Ov-ZBC MOFs reached 26.33%, significantly higher than the 10.07% in ZBC MOFs, which further confirmed the successful construction of oxygen vacancy defects in Ov-ZBC MOFs.

The existence of oxygen vacancies markedly influences the light absorption capacity and the photocatalytic properties of MOFs. As shown in Fig. 1(f), ultraviolet (UV)–vis diffuse reflectance spectra show enhanced visible-light absorption for Ov-ZBC MOFs compared to pristine ZBC, which can be ascribed to defect-induced bandgap narrowing, indicating superior photocatalytic ROS generation potential under visible-light excitation [34]. To further evaluate the ROS generation capability, EPR and chromogenic reactions involving 3,3',5,5'-tetramethylbenzidine (TMB) assay and methylene blue (MB) were employed. Figures 1(g) and 1(h) show the EPR spectra of hydroxyl radicals (·OH) and singlet oxygen ($^1O_2$) after the photocatalytic reaction. In the absence of light, no ROS signals were detected in any of the systems. Under visible light irradiation, due to the inherent catalytic properties of the MOFs, the ZBC exhibited weak ·OH and $^1O_2$ signals [35]. In contrast, Ov-ZBC showed strong characteristic peaks, indicating its higher photocatalytic ROS generation capability. The results of TMB and MB chromogenic reactions shown in Figs. 1(i) and 1(j) further confirmed this conclusion [36]. These results demonstrated that the construction of oxygen vacancy defects significantly enhanced the photocatalytic ROS generation capability of Ov-ZBC MOFs, making it a promising candidate for photodynamic antibacterial applications.

To further investigate the intrinsic mechanisms behind the enhanced photocatalytic performance of Ov-ZBC MOFs, density functional theory (DFT) calculations were performed on both ZBC and Ov-ZBC. Figures 1(k) and 1(l) show the differential charge density diagrams of the two MOFs after adsorbing the reaction substrates $H_2O$ and $O_2$. In contrast to ZBC, Ov-ZBC MOFs exhibit pronounced electron accumulation at the oxygen vacancy and significant electron depletion over the adsorbed molecules, signifying substantially enhanced interfacial charge transfer. This redistribution indicates that oxygen vacancy defects function as electron-rich active centers, which not only strengthen $H_2O$ and $O_2$ absorption but also promote their conversion to reactive oxygen species [7]. In Figs. 1(m) and 1(n), by calculating the adsorption energies for $H_2O$ and $O_2$, Ov-ZBC MOFs exhibited significantly enhanced adsorption capabilities for both substrates. $O_2$ adsorption strengthens from a weak −0.104 eV on pristine ZBC to a robust

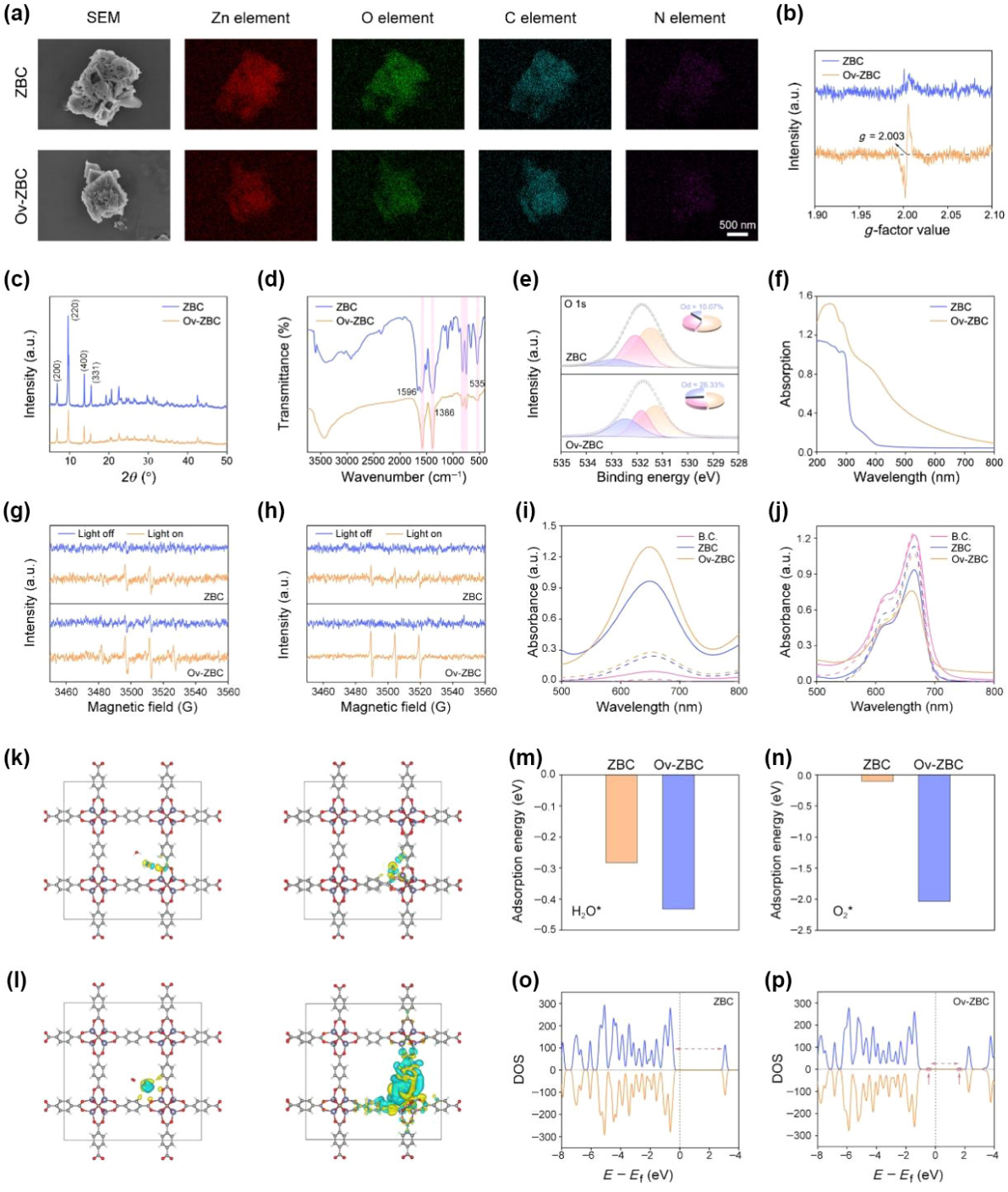


**Figure 1** The preparation and characterizations of Ov-ZBC MOFs with burst ROS production. (a) SEM images and energy dispersive X-ray spectroscopy (EDS) mapping of ZBC and Ov-ZBC MOFs. Scale bar: 500 nm. (b) EPR spectrum; (c) XRD spectrum; (d) FT-IR spectrum; (e) XPS spectrum; (f) UV–Vis spectrum; (g) EPR for detecting ·OH; (h) EPR for detecting $^1O_2$; (i) TMB assay; (j) MB assay; and (k) differential charge density maps depicting the adsorption of $H_2O$ on ZBC (left) and Ov-ZBC (right). (l) Differential charge density maps depicting the adsorption of $O_2$ on ZBC (left) and Ov-ZBC (right). (m) The $H_2O$ adsorption energy. (n) The $O_2$ adsorption energy. DOS diagrams of (o) ZBC and (p) Ov-ZBC.

−2.036 eV on Ov-ZBC, while $H_2O$ adsorption improves from −0.283 to −0.432 eV. This pronounced enhancement provides theoretical validation for the exceptional photocatalytic ROS generation performance of Ov-ZBC MOFs [37, 38]. Figures 1(o) and 1(p) show the density of states (DOS) distributions. The calculated results revealed that defect energy levels induced by oxygen vacancies appeared in Ov-ZBC at the positions indicated by the red arrows, leading to a narrowing of its bandgap and enhancing the material's light absorption capacity, which is consistent with our experimental findings. In summary, DFT calculations theoretically confirmed that the incorporation of oxygen vacancy defects effectively reduced the bandgap of Ov-ZBC MOFs, improved the separation efficiency of photogenerated carriers, and enhanced the adsorption capacity for reaction

substrates, collectively promoting the enhancement of its photocatalytic ROS generation performances.

Collectively, these results establish that oxygen vacancy engineering enhanced the ROS generation by modulating their electronic structure and light-harvesting behavior. This defect-driven enhancement in photocatalytic activity lays a mechanistic foundation for subsequent light-triggered ROS antibacterial activation and cascade therapeutic effects.

### 2.2 Light-responsive Ov-ZBC/GelMA (GOZ) integration

Like other nanomaterials, Ov-ZBC MOFs face significant constraints in biomedical applications, primarily due to their limited tissue targeting, poor bioavailability, and insufficient biodegradation [39, 40]. To solve these problems, Ov-ZBC MOFs were modified by incorporating with GelMA biopolymers to fabricate a series of composite biomaterials [41].

Figure 2(a) shows a diagram of GelMA/Ov-ZBC (GOZ) hydrogel network, and the preparation process. The mixed solution of GelMA and Ov-ZBC transformed from liquid state into solid state with the help of UV irradiation, suggesting that the hydrogels were successfully fabricated. GelMA molecules crosslinked with each other to form the hydrogel framework, while Ov-ZBC MOFs were immobilized into this framework without participating in any chemical reaction.

Herein, four kinds of hydrogels (GOZ-*n*, *n* = 0, 0.1, 0.2 and 0.3, corresponding to the content of Ov-ZBC MOFs) were fabricated. The incorporation of Ov-ZBC MOFs is supposed to modulate the physiochemical properties in a dose-dependent manner. Figure 2(b) shows the morphology of freeze-dried hydrogels. All samples exhibited a porous, spongy-like structure. The pore sizes of hydrogels decreased gradually along with an increase of Ov-ZBC content. Figures 2(c) and 2(d) show the results of hydrophilicity test. The water contact angle exhibited no significant difference among the four groups ($P > 0.05$). As shown in Fig. 2(e), the

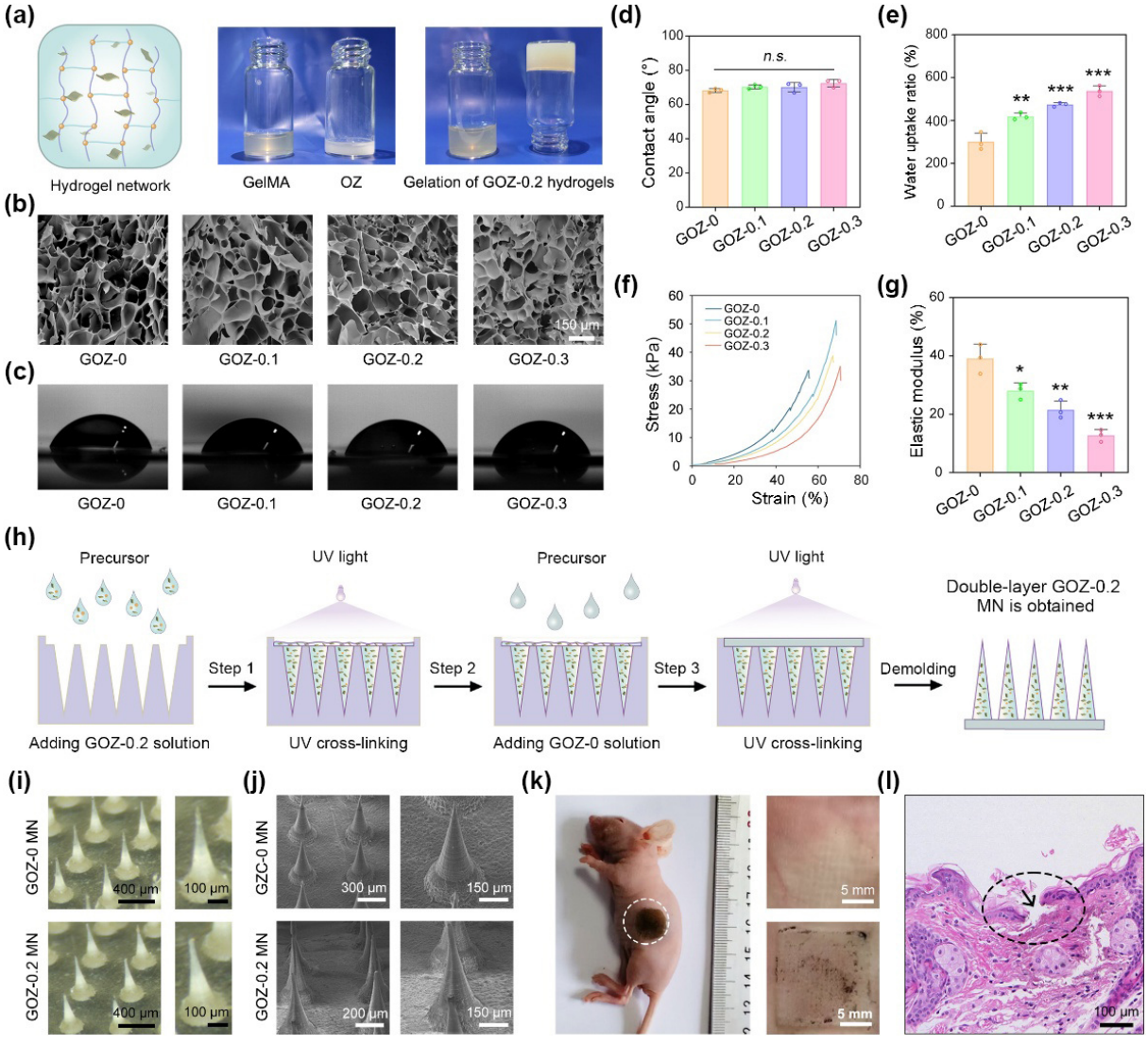


**Figure 2** The preparation and characterizations of Ov-ZBC MOFs-laden GOZ-*n* hydrogels and microneedles. (a) A diagram showing the molecular structure of GOZ-*n* hydrogels and the gelation process. (b) SEM images of freeze-dried hydrogels. Scale bar: 150 μm. (c) Optical images of water contact angle. (d) Quantitative results of contact angle ($n = 3$). (e) Water uptake ratio (%) ($n = 3$). Compression test ($n = 3$) of (f) stress and (g) elastic modulus. (h) A diagram showing the preparation process of double-layer GOZ-0.2 microneedles. (i) and (j) Morphological observations of the microneedles. Scale bars were marked. (k) and (l) GOZ-0.2 microneedles punctured into the skin tissues of nude mouse. Black arrow indicated to puncturing sites. Scale bars were marked. All data are presented as the mean ± standard deviation (SD). Statistical significance was determined using one-way ANOVA. Compared to GOZ-0 group, *n.s.* indicates no significant difference, $^*P < 0.05$, $^{**}P < 0.01$, $^{***}P < 0.001$.

equilibrium swelling ratio was 300% ± 33% for GOZ-0 group, 419% ± 13% for GOZ-0.1 group, 474% ± 7% for GOZ-0.2 group, and 537% ± 20% for GOZ-0.3 group, respectively. Significant differences were observed between GOZ-0 and other groups ($P < 0.01$).

A compression test was performed to characterize the mechanical strength of GOZ-*n* hydrogels. As shown in Fig. 2(f), the stress gradually increased as the strain increased. Among the four groups, the GOZ-0.3 group exhibited the maximum elastic deformation. The quantitative results of elastic modulus are shown in Fig. 2(g). In conclusion, the incorporation of Ov-ZBC MOFs has improved the swelling ability, but decreased the pore size and mechanical strength of composite GOZ-n hydrogels.

For transdermal delivery of Ov-ZBC MOFs, the GOZ-*n* hydrogels were further processed into microneedles. Herein, a double-layer structure of GOZ-0.2 microneedles is designed. The base layer is composed of GOZ-0 hydrogel, while the tip layer is composed of GOZ-0.2 hydrogel. As the control, the base layer and tip layer of GOZ-0 microneedles are both composed of GOZ-0 hydrogel. This approach can reduce the dosage of Ov-ZBC MOFs and improve biosafety.

As shown in Fig. 2(h), the double-layer GOZ-0.2 microneedles were prepared using a two-step mold-casting technique. As shown in Figs. 2(i) and 2(j), the microneedles were consisted of a series of tip arrays. These tips were very sharp, which is beneficial for skin puncture. The magnified images confirm that Ov-ZBC MOFs are predominantly localized within the microneedle tips, ensuring direct contact with wound tissues after insertion. This spatial distribution minimizes material loss and prevents uncontrolled diffusion, thereby establishing a confined catalytic microenvironment at the target site. Meanwhile, the transparency of the microneedle matrix allows efficient penetration of visible light, ensuring that the embedded Ov-ZBC MOFs remain photoactive after integration into the microneedle system. As shown in Figs. 2(k) and 2(l), GOZ-0.2 microneedles punctured into the skin of BALB/c nude mice, indicating that the microneedle has sufficient mechanical strength to penetrate the stratum corneum without structural failure.

To evaluate the light-responsive ion-release behavior of GOZ-0.2 microneedles, $Zn^{2+}$ release was monitored in PBS (5 mL, pH 7.4) under visible light irradiation for 24 h. As shown in Fig. S1 in the Electronic Supplementary Material (ESM), the cumulative $Zn^{2+}$ release reached 4.55 μg within 24 h, exhibiting a sustained curve with an initial rate of approximately 0.34 μg/h and then gradually decreased. This controlled release ensures a steady supply of antibacterial $Zn^{2+}$ at the wound interface, enabling continuous bacterial suppression without burst-related cytotoxicity.

Collectively, these results demonstrate that integration of light-responsive Ov-ZBC MOFs into a GelMA microneedle platform provides a synergistic strategy for spatially confined delivery and controllable catalytic activation. The Ov-ZBC/GelMA system therefore functions not merely as a passive carrier, but as an active interface that lays the groundwork for subsequent antibacterial effect and wound healing.

### 2.3 GOZ-0.2 microneedles exhibited desirable biocompatibility

As spatially localized $Zn^{2+}$ release and ROS generation may raise biosafety concerns, the biocompatibility of the microneedle system is a prerequisite for its therapeutic relevance. GOZ-0.2 microneedles were selected from the four groups for subsequent study, and their biocompatibility was evaluated, highlighting their ability for fulfilling the high requirements of class-III medical devices. The experimental design is illustrated in Fig. 3(a). For biocompatibility evaluations *in vitro*, GOZ-0.2 microneedles were co-cultured with L929 cells using a trans-well chamber [42]. For Biocompatibility evaluations *in vivo*, GOZ-0.2 microneedles were transplanted into the back skin of Sprague Dawley rats. GOZ-0 microneedles and GelMA/ZBC (GZC-0.2) microneedles served as the controls.

*In vitro* cytocompatibility assays revealed that the GOZ-0.2 microneedles exhibited negligible cytotoxicity toward representative skin-related cells at therapeutic concentration. The result of live/dead cell staining assay was shown in Figs. 3(b) and 3(c). More than 95% of cells were viable (green fluorescence), suggesting that these materials did not damage cell viability [43]. Cell migration ability was evaluated by scratch assay, as shown in Figs. 3(d) and 3(e). After 24 h of incubation, the cell migration rate was 56% ± 1.3% for blank control (B.C.) group, 44.4% ± 0.9% for GOZ-0 group, 37% ± 1.5% for GZC-0.2 group, and 40.9% ± 1.6% for GOZ-0.2 group, respectively. The GOZ-0.2 group exhibited a relatively high migration rate, further verifying its favorable cytocompatibility. These results indicated that the hydrogel matrix can effectively buffer the cell damage caused by $Zn^{2+}$ and oxidative stress while maintaining cell activity. Thus, the microneedle architecture provides a protective microenvironment that balances antibacterial activity with host cell tolerance.

The *in vivo* biosafety of the microneedle system was further assessed through histological examination of major organs and hematological analysis. Figure 3(f) shows the results of tissue-compatibility evaluations. After 14 days of transplantation, all animals exhibited no obvious pathological changes. This phenomenon suggested that the degradation products of materials will not lead to immune rejection and target organ injury. Meanwhile, as shown in Figs. 3(g)–3(l), a series of blood biochemical indexes remained within normal ranges, without significant differences observed among each group ($P > 0.05$).

Collectively, these results confirmed that the delivery of Ov-ZBC MOFs by microneedles has good biological safety. This balance between catalytic activity and biocompatibility establishes a critical foundation for the subsequent antibacterial efficacy and wound healing.

### 2.4 Two-hit antibacterial effect under visible light

Herein, it is hypothesized that the GOZ-0.2 microneedle system would trigger a synergistic antibacterial function under visible light irradiation that integrates metal ion-mediated toxicity with ROS. To validate this hypothesis, the antibacterial performance in response to *E. coli* and *S. aureus* was systematically investigated under light conditions.

As shown in Figs. 4(a) and 4(b), GOZ-0.2 group exhibits pronounced antibacterial efficacy against both *S. aureus* and *E. coli* ($P < 0.001$) under visible light irradiation. Although GZC-0.2 group also had antibacterial effect, it was significantly weaker than that of GOZ-0.2 group. It was concluded that both the ROS and $Zn^{2+}$ ions played a vital role in the antibacterial ability of GOZ-0.2 microneedles.

Notably, compared to GOZ-0.2 group, GOZ-0.2 + VC group and GOZ-0.2 + EDTA group exhibited enhanced bacterial survival ability. Anti-oxidative vitamin C (VC) functioned as an antagonist of ROS, and ethylenediaminetetraacetic acid (EDTA) functioned as

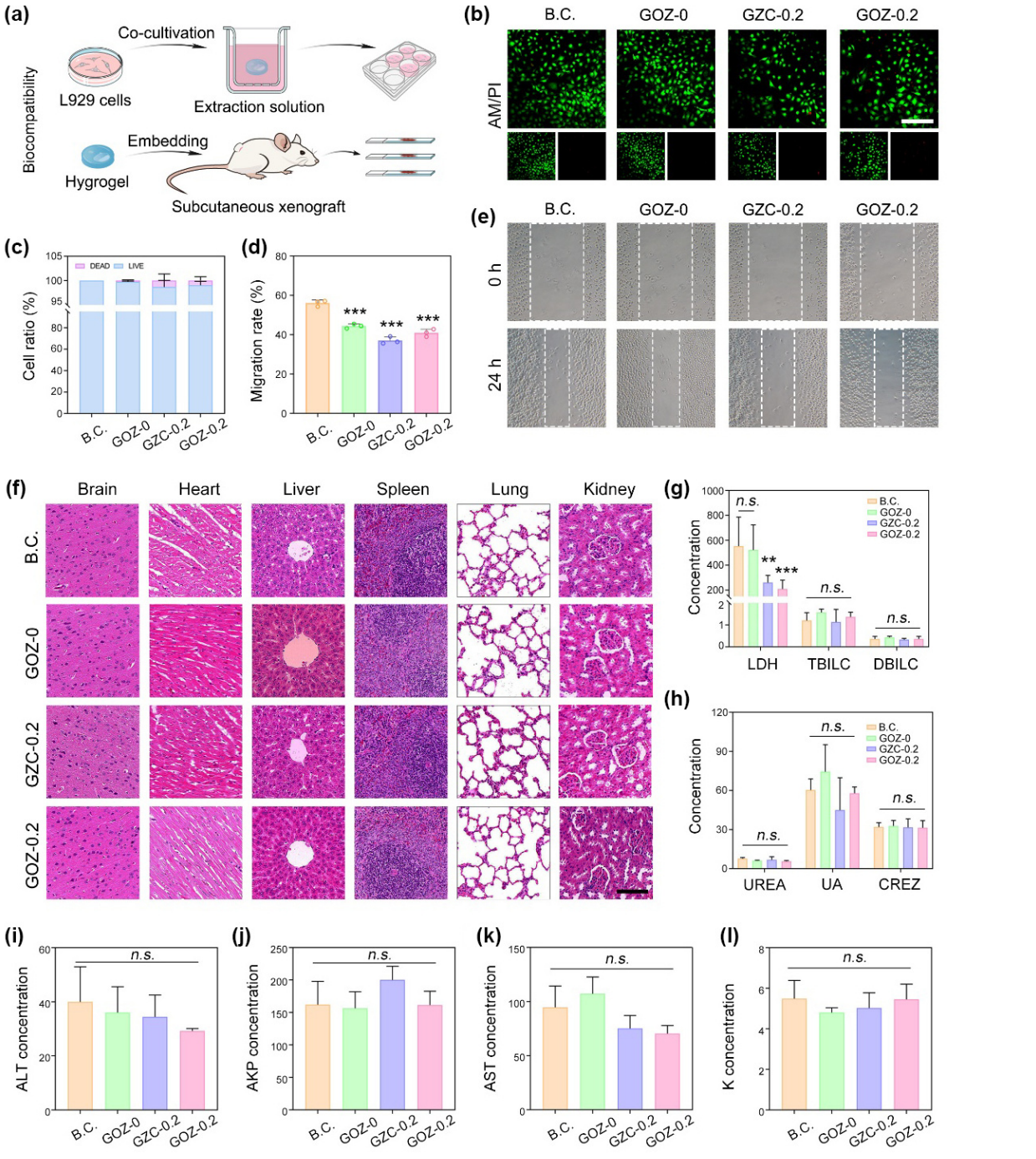


**Figure 3** Biocompatibility evaluations of the GOZ-0.2 microneedles. (a) A diagram showing the experimental methods of biocompatibility evaluations *in vitro* and *in vivo*. (b) Live/dead cell staining assay and (c) quantitative analysis ($n$ = 3). Scale bar: 200 μm. (d) The quantitative analysis and (e) the images of cell scratching assay ($n$ = 3). (f) H&E staining images of the organs. Scale bar: 100 μm; (g)–(l) a series of blood biochemical was tested, including ALT, AKP, AST, and $K^+$ ($n$ = 3). All data are presented as the mean ± SD. Statistical significance was determined using one-way ANOVA. Compared to B.C. group, *n.s.* indicates no significant difference, $^{**}P < 0.01$, $^{***}P < 0.001$.

a chelating agent of $Zn^{2+}$ ions [44, 45]. This phenomenon revealed that neither ROS nor $Zn^{2+}$ ions toxicity alone is sufficient to account for the observed bactericidal performance, further substantiating the cooperative involvement of $Zn^{2+}$ ions and ROS antibacterial function [46]. Figures 4(c) and 4(d) show the proliferation curves of *S. aureus* and *E. coli*, respectively. Similarly, while GOZ-0.2 microneedles exhibited a significant suppressive effect on bacterial proliferation, this activity was partially rescued by VC and EDTA. Correspondingly, the bacterial morphology obviously shrank after GOZ-0.2 treatment, owing to the destruction of bacterial cell membrane, as evidenced by morphological disruption observed by electron microscopy in Fig. 4(e) [47, 48].

Collectively, these findings establish that visible light irradiation activates a synergistic two-hit antibacterial mechanism in GOZ-0.2 microneedles, coupling photocatalytic ROS generation with sustained $Zn^{2+}$ release. GOZ-0.2 microneedles demonstrated good

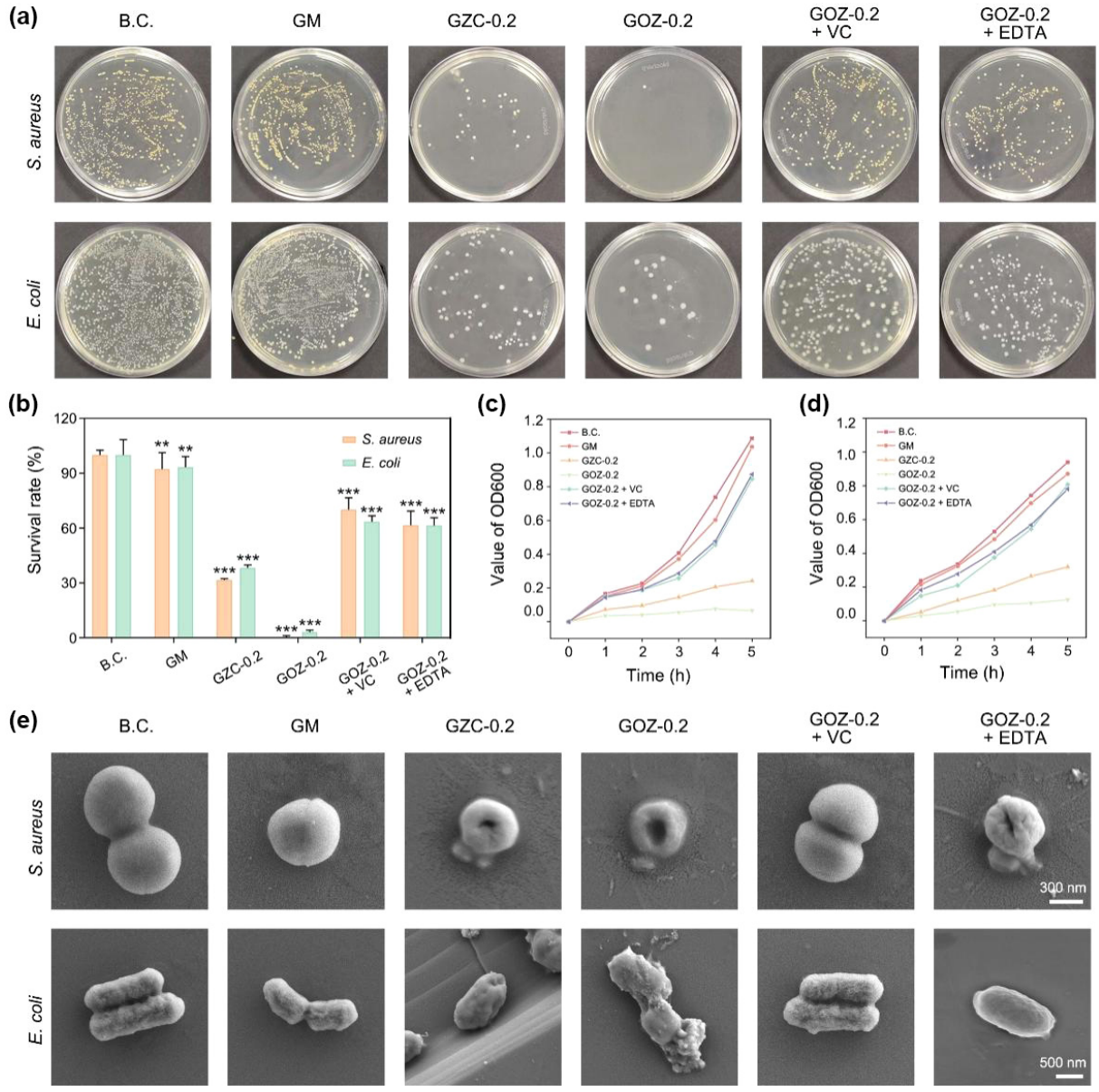


**Figure 4** Broad-spectrum anti-bacterial evaluations of the GOZ-0.2 microneedles. (a) Bacterial clone formation assay and (b) the quantitative results ($n$ = 3). (c) Bacterial proliferation curves of *S. aureus* ($n$ = 1). (d) Bacterial proliferation curves of *E. coli* ($n$ = 1). (e) Bacterial morphology observation by SEM. Scale bars: 300 nm (up) or 500 nm (bottom). All data are presented as the mean ± SD in panel (b). Statistical significance was determined using one-way ANOVA. Compared to B.C. group, $^{**}P < 0.01$, $^{***}P < 0.001$.

broad-spectrum antibacterial activity, which will be extensively applied in biomedical fields, particularly wound healing.

### 2.5 GOZ microneedles accelerated infected wound healing

In this chapter, a full thickness skin defect model was established to evaluate the pro-regeneration effect of GOZ microneedles. Figure 5(a) shows the experimental plans. For the GOZ group, the rats were infected with *S. aureus*, and immediately treated with GOZ-0.2 microneedles and visible light irradiation. Commercial products (3M group) served as positive control, and neat GOZ-0 microneedles (GM group) and GZC-0.2 microneedles (GZC group) served as negative controls. Blank control (B.C.) group was not treated. The rats were conventionally fed for another 14 days to allow skin regeneration.

As shown in Fig. 5(b), the wound sites were dynamically monitored. Wounds treated with light-activated GOZ microneedles exhibit significantly accelerated closure compared to control groups. The quantitative results of wound healing rate are shown in Figs. 5(c)–5(f). At day 3, the healing rate was 17.49% ± 3.8% for B.C. group, 30.6% ± 5.6% for 3M group, 18.9% ± 3.1% for GM group, 26.8% ± 4.7% for GZC group, and 42.5% ± 2.8% for GOZ group, respectively. Compared with B.C. group, GOZ group exhibited significant differences ($P < 0.001$). Similar trends were found at days 6, 9 and 12. Thus, GOZ group healed fastest among five groups. It was concluded that the pro-regeneration effect of GOZ microneedles was better than that of commercial products (3M).

Figure 5(g) shows the fluorescent images of ROS in wound tissue, which was labelled by 2',7'-dichlorodihydrofluorescein

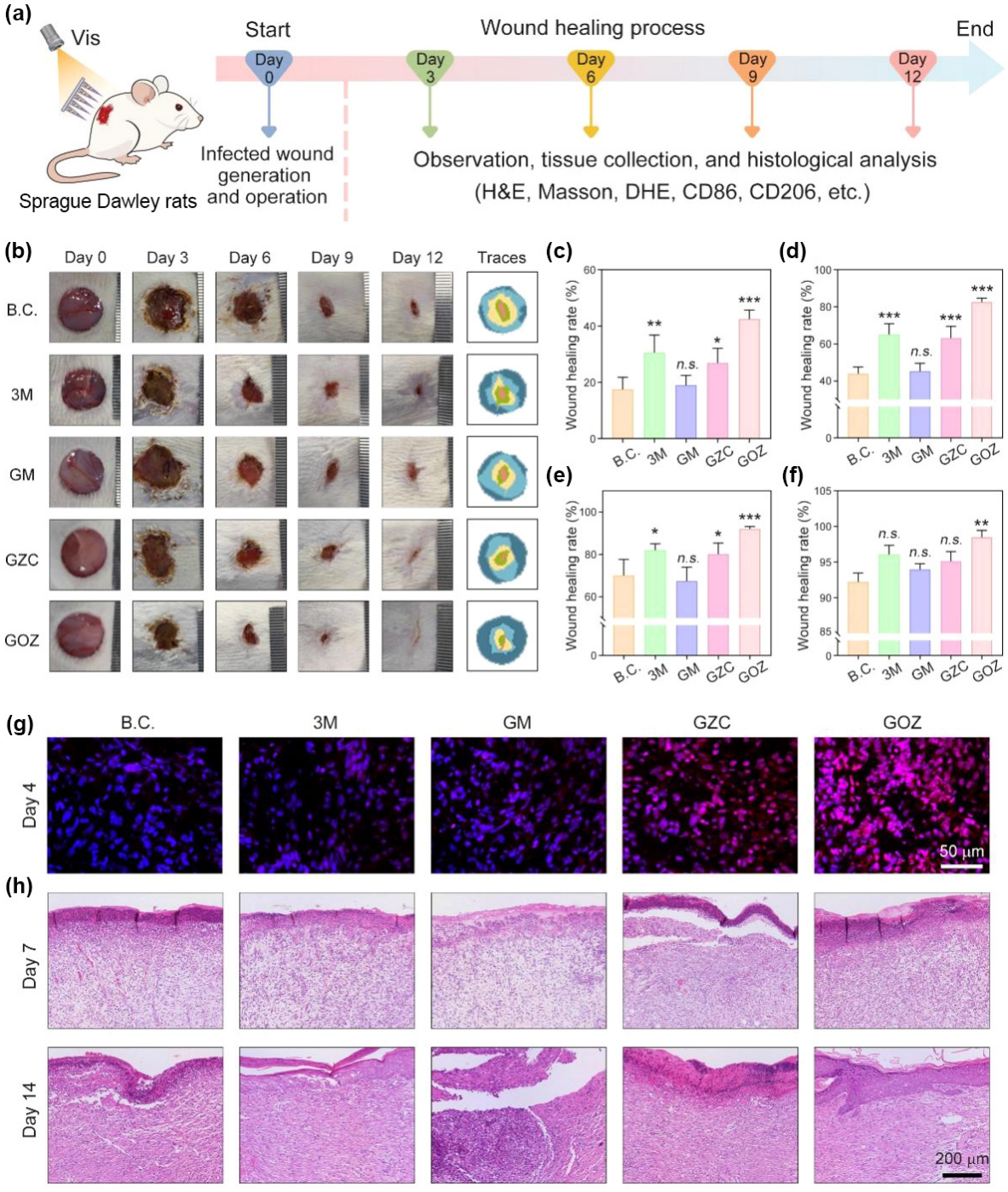


**Figure 5** Accelerated wound healing by GOZ microneedles in bacterial-infected Sprague Dawley rats. (a) A diagram showing the experimental plan. (b) Traces of wound healing process. Quantitative results of wound healing rate at days (c) 3, (d) 6, (e) 9, and (f) 12, respectively ($n$ = 6). (g) DCFH-DA staining images at day 4. Scale bar: 50 μm. (h) H&E staining images at days 7 and 14, respectively, scale bar: 200 μm. All data are presented as the mean ± SD. Statistical significance was determined using one-way ANOVA. Compared to B.C. group, $^{*}P < 0.05$, $^{**}P < 0.01$, $^{***}P < 0.001$.

diacetate (DCFH-DA). Compared to B.C. group, a markedly enhanced ROS signal is observed in wounds treated with GOZ microneedles under visible light irradiation. This elevated fluorescence intensity can be attributed to the incorporation of oxygen vacancy, endowing the Ov-ZBC MOFs with enhanced pro-oxidative potential. Rather than serving as a standalone therapeutic factor, the localized ROS burst functions as an upstream trigger for antibacterial activation, facilitating rapid bacterial clearance and subsequent modulation of the wound microenvironment. Thus, the ROS signal exists spatially confined to the wound region, indicating localized activation rather than systemic oxidative stress [49]. This controlled ROS release contributes to the accelerated wound healing treated with GOZ microneedles.

To further verify the antibacterial efficacy at the wound site, bacterial burden was evaluated by plate colony counting. As shown in Fig. S2 in the ESM, wounds treated with GOZ microneedles

exhibited a markedly reduced number of viable bacterial colonies compared with the B.C. group, indicating efficient suppression of bacterial survival in wounds. These results confirm that GOZ microneedles effectively eradicate bacterial infection at the wound site, which contributes to the establishment of a favorable microenvironment for subsequent tissue regeneration.

Hematoxylin and eosin (H&E) staining images of neo-skin tissues shown in Fig. 5(f) further revealed that complete keratinized epithelium was found in 3M and GOZ groups at day 14, indicating that the wound healing process was almost completed [50]. Meanwhile, less inflammation cells infiltrated in GOZ group, partially owning to the antibacterial activity [51]. The ROS played a vital role in eliminating bacterial infection and inhibiting inflammatory response [52, 53]. Our results have confirmed the pro-regeneration effect of GOZ-0.2 microneedles.

As shown in Fig. 6(a), the wound healing process is divided into several phases (time points). At each phase, several key biological events occur to drive the wound repair process and promote skin tissue regeneration [54, 55]. To gain insight into the molecular mechanism underlying the observed healing outcomes, a series of immunofluorescence staining assays were performed to characterize these key regenerative and immune-related markers in wound tissues.

Figure 6(b) shows the immunofluorescence analysis of myeloperoxidase (MPO) and CD11b at day 4. MPO predominantly exists in neutrophils and monocytes, while CD11b is one of the biomarkers of the myeloid innate immune cell population, particularly monocytes, macrophages, and neutrophils [56]. They are commonly used as the indicators of inflammation intensity. In this study, both the expression of MPO and CD11b in GOZ group got significantly decreased compared to B.C. group ($P < 0.001$), indicating effective attenuation of acute inflammatory responses. This reduction in inflammation correlates temporally with rapid bacterial clearance, suggesting that antibacterial intervention plays a significant role in reshaping the immune microenvironment.

As shown in Figs. 6(c) and 6(d), the total macrophages (marked

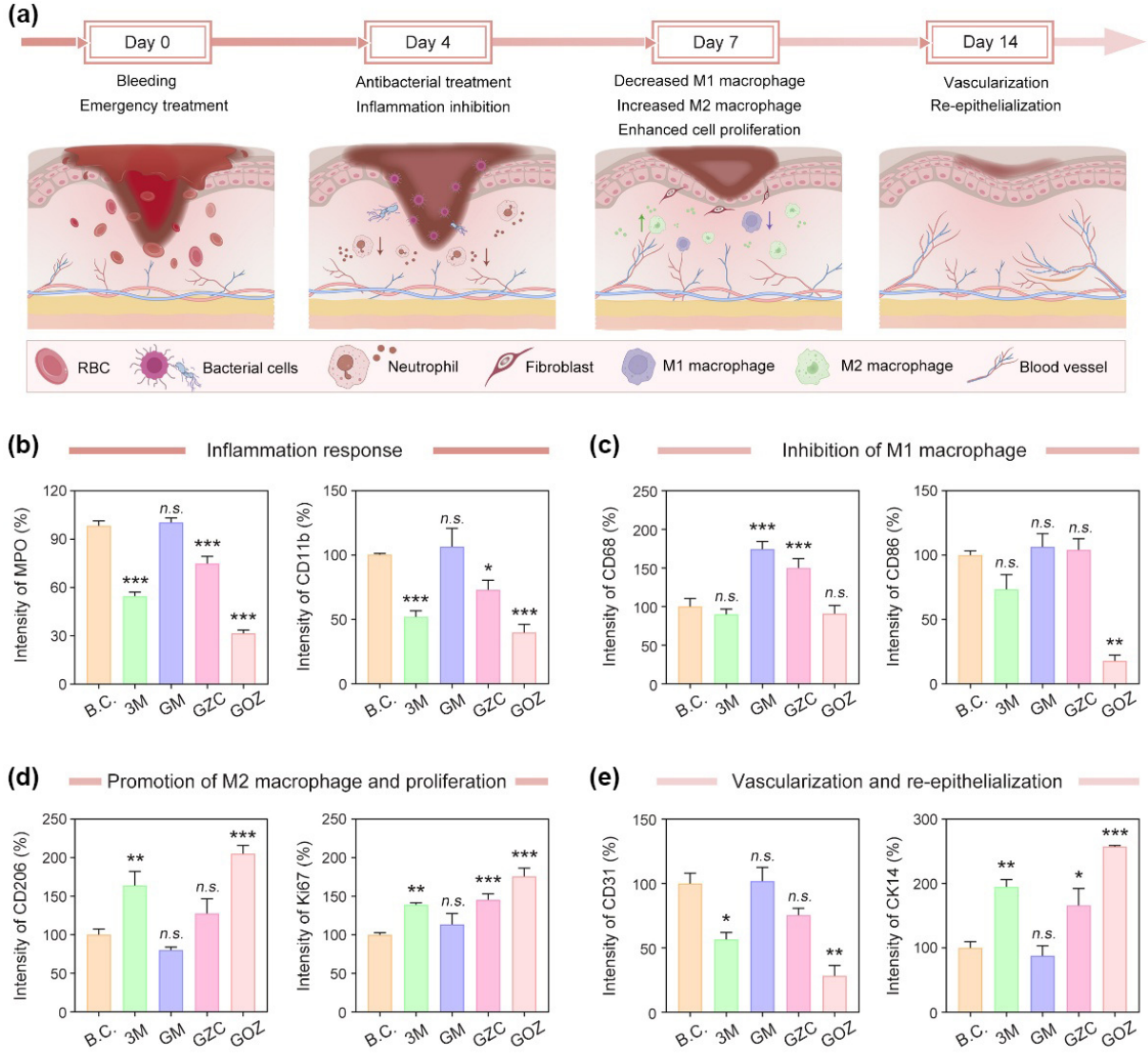


**Figure 6** Mechanism insight into accelerated wound healing. (a) A diagram showing the key events during wound healing process. (b) Quantitative results of MPO and CD11b staining assay at day 4 ($n = 3$). (c) CD68 and CD86 staining assay at day 7 ($n = 3$). (d) CD206 and Ki67 staining assay at day 7 ($n = 3$). (e) CD31 and CK14 staining assay at day 14 ($n = 3$). All data are presented as the mean ± SD. Statistical significance was determined using one-way ANOVA. Compared to B.C. group, *n.s.* indicates no significant difference, $^{*}P < 0.05$, $^{**}P < 0.01$, $^{***}P < 0.001$.

by CD68), M1 macrophages (marked by CD86), M2 macrophages (marked by CD206), and cell proliferation (marked by Ki67) were characterized at day 7 [57]. Compared to B.C. group, GOZ group exhibited no significant difference in terms of total macrophage ($P > 0.05$). However, GOZ group exhibited less M1 macrophages, but more M2 macrophages. This macrophage polarization is consistent with the establishment of a pro-healing immune microenvironment that favors tissue repair rather than prolonged inflammatory response. Yan et al. has summarized the differentiated functions of M1 and M2 macrophages in modulating the wound healing process [58]. Usually, the more M2 macrophages there are, the more pro-regenerative cytokines they produced. Thus, the cell proliferation accelerated *in situ*.

Tissue remodeling occurred at the later stage of wound healing [59, 60]. At this phase, the wall of blood vessels contracts, the number decreases, and internal blood begins to flow, indicating the maturation of neo-blood vessels. Meanwhile, epithelial cells highly express CK14, and establish a tight junction with the dermis layer as a physical barrier. As shown in Fig. 6(e), the vascularization and re-epithelialization at day 14 were labelled by CD31 and CK14, respectively. Compared to B.C. group, the expression of CD31 in GOZ group got significantly decreased, while that of CK14 got significantly increased. Importantly, rather than indicating impaired angiogenesis, the decreased CD31 expression suggests a transition from early inflammatory neovascularization toward vascular maturation and stabilization, a hallmark of advanced wound remodeling [61]. Meanwhile, the increased CK14 expression confirms enhanced re-epithelialization and restoration of epidermal integrity, contributing to the formation of a functional skin barrier.

In conclusion, the GOZ-0.2 microneedles efficiently accelerated *S. aureus*-infected wound healing via multiple mechanisms, including but were not limited to anti-inflammatory, broad-spectrum antibacterial activity, promotion of M2 macrophage polarization, cell proliferation and re-epithelialization.

## 3 Conclusions

In summary, this study presents a defect-engineered, light-activated microneedle platform that achieves efficient treatment of infected wounds. An oxygen vacancy-rich Ov-ZBC MOF was designed to enhance visible-light-driven ROS generation, and their integration into a GelMA microneedle system enabled precise transdermal delivery and spatially confined catalytic activation with favorable biocompatibility. Under visible light irradiation, GOZ-0.2 microneedles initiate a synergistic two-hit antibacterial mechanism by combining photocatalytic ROS production with sustained $Zn^{2+}$ ions release, efficiently inhibiting the survival and proliferation of both gram-positive *S. aureus* and gram-negative *E. coli*, suggesting desirable broad-spectrum antibacterial activity. GOZ-0.2 microneedles significantly accelerated the wound healing process in an *S. aureus*-infected full thickness skin defect model. The pro-regeneration mechanisms were revealed, including but not limited to anti-inflammatory, broad-spectrum antibacterial activity, promotion of M2 macrophage polarization, cell proliferation and re-epithelialization. More importantly, the application effect of GOZ-0.2 microneedles was better than that of commercial wound dressings from the 3M Co., Ltd. This study confirmed that the strategy of Ov-based defect engineering combined with microneedle-mediated transdermal delivery is an efficient and biocompatible strategy to modify Zn-based MOFs for advanced biomedical applications.

## 4 Experimental

### 4.1 Materials

Zinc acetate dihydrate ($Zn(CH_3COO)_2{\cdot}2H_2O$) and *N*,*N*-dimethylformamide (DMF) were obtained from Sinopharm Chemical Reagent Co., Ltd. (Shanghai, China). Terephthalic acid ($H_2BDC$), polyvinyl pyrrolidone (PVP), 2-aminoterephthalic acid ($NH_2$-BDC) were obtained from Aladdin Scientific Co., Ltd. (Shanghai, China). Gelatin, methacrylic anhydride (MA), 2,2,6,6-tetramethylpiperidine (TEMP), and 5,5-dimethyl-1-pyrroline *N*-oxide (DMPO) were obtained from Macklin Inc. (Shanghai, China). MB and TMB were obtained from MCE Biotech. Co., Ltd. (New Jersey, USA). Mouse fibroblasts (L929 cells), *E. coli* strain and *S. aureus* strain were kindly provided by the Medical Research Center, Zhongnan Hospital of Wuhan University. Cell medium, trypsin, fetal bovine serum (FBS), and phosphate-buffered saline (PBS) were purchased from Thermo-Fisher Scientific Inc. (Shanghai, China). Cell apoptosis kit, ROS staining assay kit, and bacterial live/dead staining kit were purchased from Beyotime Biotech. Co., Ltd. (Shanghai, China). Other chemicals and commercial kits were used as received.

### 4.2 Synthesis of ZBC MOFs and Ov-ZBC MOFs

A hydrothermal reaction was used for synthesizing ZBC MOFs. Briefly, 277 mg of PVP powder was dissolved into 37.5 mL of DMF, and then mixed with 10 mL of 20 mM $H_2BDC$ solution. The mixture was heated to 90 °C for 15 min, followed by adding 2.5 mL of 160 mM $Zn(CH_3COO)_2{\cdot}2H_2O$ solution. Under constant stirring, the reaction occurred at 90 °C for another 2 h. After cooling to room temperature, ZBC MOFs were obtained by centrifugation, rinsed with distilled water for 3 times, and vacuum-dried for further study.

Ov-ZBC MOFs were fabricated according to a previous report with minor modifications. The precursor solution of $H_2BDC$ was replaced by a mixture of $H_2BDC$ and $NH_2$-BDC with a mole ratio of 3: 1. The ZBC MOFs were synthesized using the same protocols, and then calcined in a muffle furnace (M10, Sigma, Shanghai) at 315 °C for 1 h to obtain Ov-ZBC MOFs.

### 4.3 Preparation of composite hydrogels and microneedles

Gelatin was chemically modified to prepare GelMA with a substitution degree of 29.1% [62]. Ov-ZBC MOFs were mixed with 15 wt% GelMA solution, and UV-crosslinked to prepare a series of composite GOZ-*n* hydrogels ($n = 0$, 0.1, 0.2, and 0.3, corresponding to the weight percentage of Ov-ZBC). The codes, compositions and preparation parameters of GOZ-*n* hydrogels are listed in Table 1. These hydrogels were further processed into double-layer microneedles using a two-step mold-casting technique. More information about the preparation methods of composite hydrogels

**Table 1** The codes, compositions and preparation parameters of GOZ-*n* hydrogels

| | System (mL) | GelMA (g) | GOZ (mg) | 10% 2959 (μL) | UV time (min) |
|---|---|---|---|---|---|
| GOZ-0 | 10 | 1.5 | 0 | 200 | 5 |
| GOZ-0.1 | 10 | 1.5 | 10 | 200 | 5 |
| GOZ-0.2 | 10 | 1.5 | 20 | 200 | 5 |
| GOZ-0.3 | 10 | 1.5 | 30 | 200 | 5 |

and double-layer microneedles could be found in our previous reports [19, 20].

### 4.4 Physicochemical characterizations

The morphology of MOFs was observed using an SEM (Sigma 300, ZEISS, Germany) equipped with an EDS mapping. The chemical compositions of MOFs were characterized by XRD (Smart-Lab SE, Rigaku, Japan), FT-IR (Nicolet iS 10, Thermo-Fisher, USA), XPS (K-Alpha, Thermo-Fisher, USA), and UV–Vis (K-Alpha, Thermo-Fisher, USA). The oxygen vacancy was identified by EPR (ELEXSYS E580, Bruker, Germany). These characterizations were performed with the kind help from Yan-Qu Information Techno. Co., Ltd. (Hangzhou, China).

### 4.5 Swelling and water contact angle test

The GOZ-*n* hydrogels were cut into 1 $cm^3$ cubes, freeze-dried, and immersed into distilled water for 48 h. The dry weight and wet weight of the hydrogels were tested for measuring the equilibrium swelling rate. The water contact angle of dried hydrogels was tested using a dynamic video acquisition system (OCA25, Dataphysics, Germany). The droplet was set to 2 μL. At least three independent samples were used for statistical analysis.

### 4.6 Compression test

The GOZ-*n* hydrogels were cut into cylinders with a diameter of 5 mm and a height of 12 mm. A universal material testing machine (UTM4102S, SUNS, China) was used for compression test. The compression rate was set to 2 mm/min, and the maximum compression deformation was set to 90%. The elastic modulus of the hydrogels was calculated as previously reported [63].

### 4.7 $Zn^{2+}$ releasing test

The GOZ-0.2 hydrogel was placed in a 15 mL centrifuge tube, 5 mL release medium (PBS, pH 7.4) was added, and the hydrogel was shaken at 37 °C and 50 rpm under visible light irradiation (25 mW/$cm^2$, 400–700 nm, Zolix SS-150). 0.5 mL of the solution was removed at 0.5, 3, 6, 12, and 24 h, and the equal volume of blank medium preheated at 37 °C was immediately filled. The samples were filtered by 0.22 μm needle filter and acidified by 1% (v/v) $HNO_3$. The $Zn^{2+}$ concentration was determined by inductively coupled plasma optical emission spectrometry (ICP-OES) (Agilent 510, 213.857 nm).

### 4.8 Skin puncturing test

This study was performed with the approval of Animal Welfare and Ethics Committee of Hubei University (20240034). BALB/c nude mice were purchased from Shu-Bei-Li Biotech. Co., Ltd. (Wuhan, China), and safely anesthetized by isoflurane inhalation. The GOZ-0.2 microneedles were placed on the skin with compression. The skin images before and after skin puncturing were captured. According to standard protocols, the skin tissues were harvested for H&E staining analysis.

### 4.9 Biocompatibility evaluations

Biocompatibility evaluations *in vitro*: A trans-well chamber was used for cell-based biocompatibility evaluations. L929 cells were co-cultured at the lower layer of trans-well chamber, and the materials were placed onto the upper layer of trans-well chamber. The transport of substances occurred through the pores on the trans-well membranes. According to the previous reports [64, 65], the viability and migration of treated L929 cells were evaluated by live/dead cell staining assay and scratching assay, respectively.

Biocompatibility evaluations *in vivo*: Female Sprague Dawley rats, weighting about 180 g, were randomly divided into four groups ($n$ = 3). After anesthetized by isoflurane inhalation, the microneedles were transplanted into the back skin of each animal for 14 days. The B.C. group was sham-operated. After that, the animals were anesthetized again. Fresh whole blood was collected for a series of blood biochemical tests, and the organs (brain, heart, liver, spleen, lung, kidney) were collected and fixed with 4 wt% paraformaldehyde solution for H&E staining analysis.

### 4.10 Antibacterial evaluations

The broad-spectrum antibacterial activity of the microneedles was evaluated using both gram-negative *E. coli* stain and gram-positive *S. aureus* stain as model organisms. The proliferation-active bacteria were collected by centrifugation, and then suspended into 0.85% normal saline for blocking bacterial proliferation. The bacterial suspension was co-cultured with the materials and visible light irradiation (25 mW/$cm^2$, 400–700 nm, Zolix SS-150) for another 4 h. For the positive control groups, VC and EDTA were added into the suspension to rescue the antibacterial effects. After that, the proliferation and survival ability of treated bacteria were evaluated as follows:

Proliferation assay: The treated bacteria were seeded into 5 mL of Luria-Bertani (LB) liquid medium, and then cultured at 37 °C with constant stirring. At regular time points, 2 μL of bacterial suspension was sampled. The absorbance value at 600 nm was detected using a NanoDrop (One$^C$, Thermo-Fisher, USA).

Clone formation assay: The treated bacteria were seeded onto LB solid medium, and incubated overnight to allow the formation of bacterial clones. The images of bacterial clones were captured using a digital camera (iPhone 16, Apple, USA). The number of bacterial clones was counted with the help of Image J software.

SEM observation: The treated bacteria were fixed with glutaraldehyde solution, and then de-hydrated using gradient alcohol solution. After coated with a gold layer, the bacteria were observed by SEM.

### 4.11 Wound healing evaluations

Thirty female Sprague Dawley rats were fed in specific pathogen free (SPF) environment for 7 days to minimize any stress, and then divided randomly into five groups ($n$ = 6), including B.C. group, product (3M) group, GM group, GZC group and GOZ group. All animals were safely anesthetized, while the hair on their backs was removed using a razor. The round skin wounds with a diameter of 15 mm were created in each rat, infected with *S. aureus* suspension, and immediately covered with a piece of materials (including the microneedles or commercial products). All the animals were regularly treated with visible light irradiation (25 mW·$cm^{-2}$, 400–700 nm, Zolix SS-150) and fed for another 14 days to allow skin wound healing.

At regular time points, the images of wound sites were captured, and their area was manually measured. Fresh neo-skin tissues were also collected for a series of histological analysis, such as H&E staining and immunofluorescence staining (MPO, CD11b, CD86, CK14). Histological analysis was performed with the help of qualified FBER Biotech. Co., Ltd. (Wuhan, China).

### 4.12 Statistical analysis

One-way analysis of variance (ANOVA) was employed for

statistical analysis. Quantitative data are expressed as mean ± SD. At least three independent samples were included. Statistical significance was defined as $^{*}P < 0.05$, $^{**}P < 0.01$, and $^{***}P < 0.001$.

**Electronic Supplementary Material**: Supplementary material (further details of Zinc ions releasing and bacterial clone assay) is available in the online version of this article at https://doi.org/10.26599/NR.2026.94908545.

## Data availability

All data needed to support the conclusions in the paper are presented in the manuscript and the Electronic Supplementary Material. Additional data related to this paper may be requested from the corresponding author upon request.

## Acknowledgements

This work was supported by National Major Difficult Disease Clinical Collaboration Project between Traditional Chinese and Western Medicine (No. ZDYN-2024-A-18), Jichu-Zhongnan Joint Construction Project of Wuhan University (No. JCZN2025001), and Open Research Fund of Hubei Key Laboratory of Urological Diseases (Nos. MNXTJB202401 and MNXTJB202404).

## Declaration of competing interest

The authors declare that they have no conflict of interest.

## Author contribution statement

W. W. C., and W. W.: Experimental design, validation, visualization, data curation, writing manuscript. Z. J. Z., H. Y., and Y. Y.: Experimental design, validation, visualization. F. X., W. J. Y., and Z. S. C: Experimental design, methodology. W. K. H., X. Y. X., and Z. J. W.: Supervision, funding acquisition, project administration, review & editing. All the authors have approved the final manuscript.

## Informed consent

Not applicable.

## Ethics statement

This study was performed with the approval of Animal Welfare and Ethics Committee of Hubei University (Ethics code: 20240034).

## Use of AI statement

None.

## References

[1] Uberoi, A.; McCready-Vangi, A.; Grice, E. A. The wound microbiota: Microbial mechanisms of impaired wound healing and infection. *Nat. Rev. Microbiol.* **2024**, *22*, 507–521.

[2] Zare, I.; Zahed Nasab, S.; Rahi, A.; Ghaee, A.; Koohkhezri, M.; Ramezani Farani, M.; Madadi Gholipour, H.; Atabaki, A. H.; Hamblin, M. R.; Mostafavi, E. et al. Antimicrobial carbon materials-based quantum dots: From synthesis strategies to antibacterial properties for diagnostic and therapeutic applications in wound healing. *Coord. Chem. Rev.* **2025**, *522*, 216211.

[3] Wang, Z. J.; Liang, X.; Wang, G. Y.; Wang, X. H.; Chen, Y. Emerging bioprinting for wound healing. *Adv. Mater.* **2025**, *37*, e2304738.

[4] Li, Q. Y.; Li, B. W.; Yang, R.; Chen, X. H.; Shang, C. X.; Feng, G. Q.; Wu, Z. Y.; Teng, Y.; He, H. N.; Bai, Y. et al. Photosynthesis pneumatic patch promoted deep-wound healing. *Cell Biomater.* **2025**, *1*, 100047.

[5] Zang, Y.; Zhang, W.; Wang, W. Q.; Zhao, X. Y.; Wang, X. W. TiO/CIP/SilMA hydrogels promote the repair of infected wounds by interfering with bacterial signaling and energy metabolism. *Cell Biomaterials,* **2026**, *2*, 100217

[6] Gao, L. Z.; Zhuang, J.; Nie, L.; Zhang, J. B.; Zhang, Y.; Gu, N.; Wang, T. H.; Feng, J.; Yang, D. L.; Perrett, S. et al. Intrinsic peroxidase-like activity of ferromagnetic nanoparticles. *Nat. Nanotechnol.* **2007**, *2*, 577–583.

[7] He, X. J.; Lv, Y.; Lin, Y. L.; Yu, H.; Zhang, Y. P.; Tong, Y. H.; Zhang, C. W. Platinum nanoparticles regulated $V_2C$ MXene nanoplatforms with NIR-II enhanced nanozyme effect for photothermal and chemodynamic anti-infective therapy. *Adv. Mater.* **2024**, *36*, 2400366.

[8] Muhammad, P.; Zada, A.; Rashid, J.; Hanif, S.; Gao, Y. N.; Li, C. C.; Li, Y. Y.; Fan, K. L.; Wang, Y. L. Defect engineering in nanocatalysts: From design and synthesis to applications. *Adv. Funct. Mater.* **2024**, *34*, 2314686.

[9] He, W. Y.; Wu, J. H.; Liu, J. L.; Li, J. Single-atom nanozymes for catalytic therapy: Recent advances and challenges. *Adv. Funct. Mater.* **2024**, *34*, 2312116.

[10] Zhang, D. D.; Chen, Q.; Ren, Q. X.; Zhong, W. B.; Zhang, H. J.; Wang, G. N.; Zhang, Y. Transition metal-based nanozymes: Classification, catalytic mechanisms and emerging biomedical applications. *Coord. Chem. Rev.* **2024**, *508*, 215771.

[11] Zhang, Q.; Jiang, S.; Lv, T. T.; Peng, Y.; Pang, H. Application of conductive MOF in zinc-based batteries. *Adv. Mater.* **2023**, *35*, 2305532.

[12] Bhakare, M. A.; Likhite, V. V.; Bhosale, K. L.; Lokhande, K. D.; Bondarde, M. P.; Dhumal, P. S.; Degani, M.; Some, S. Synthesis of a dual-functional fluorescent zinc-based metal organic framework for antibacterial and anti-counterfeit ink applications. *J. Indian Chem. Soc.* **2025**, *102*, 101898.

[13] N.; Cai, K.; Zhao, J. W.; Liu, C. C.; Li, H. H.; Tan, P.; Li, Y.; Li, D. F.; Ma, X. Mannosylated MOF encapsulated in *Lactobacillus* biofilm for dual-targeting intervention against mammalian *Escherichia coli* infections. *Adv. Mater.* **2025**, *37*, 2503056.

[14] Yuan, M.; Kermanian, M.; Agarwal, T.; Yang, Z.; Yousefiasl, S.; Cheng, Z. Y.; Ma, P. A.; Lin, J.; Maleki, A. Defect engineering in biomedical sciences. *Adv. Mater.* **2023**, *35*, 2304176.

[15] Han, D.; Li, X. G.; Zhang, L. B. Recent advancements for defect engineering in nanozymes. *Coord. Chem. Rev.* **2026**, *546*, 217067.

[16] S. S.; Liu, X. S.; Wu, Y.; Huang, H.; Song, X. R.; Feng, W.; Dai, X. Y.; Chen, Y. Defect-engineered sonopiezoelectric nanosheets enable sacrificial-agent-free hydrogen peroxide self-cycling for enhanced pancatalytic therapy. *Cell Biomater.* **2025**, *1*, 100101.

[17] Dong, H. J.; Zhou, Y. Y.; Wang, L. L.; Chen, L.; Zhu, M. S. Oxygen vacancies in piezocatalysis: A critical review. *Chem. Eng. J.* **2024**, *487*, 150480.

[18] Gao, Y.; Liu, S. Q.; Liu, H.; Ge, H. Y.; Zhang, M.; Zhao, C. Y.; Gong, Y. F.; Zhang, X. Y.; Wang, C.; Sun, X. et al. Application of oxygen vacancy defects in enhanced anti-cancer nanomedicine. *Sci. China Chem.* **2023**, *66*, 2492–2512.

[19] You, W. J.; Cai, Z. C.; Xiao, F.; Zhao, J. X.; Wang, G. Y.; Wang, W.; Chen, Z. S.; Hu, W. K.; Chen, Y.; Wang, Z. J. Biomolecular microneedle initiates $Fe_3O_4$/MXene heterojunction-mediated nanozyme-like reactions and bacterial ferroptosis to repair diabetic wounds. *Adv. Sci.* **2025**, *12*, 2417314.

[20] Wang, G. Y.; Wang, W.; Chen, Z. S.; Hu, T.; Tu, L. F.; Wang, X. L.;

Hu, W. K.; Li, S.; Wang, Z. J. Photothermal microneedle patch loaded with antimicrobial peptide/$MnO_2$ hybrid nanoparticles for chronic wound healing. *Chem. Eng. J.* **2024**, *482*, 148938.
[21] Zhou, Z. P.; Deng, T.; Tao, M. X.; Lin, L. S.; Sun, L. Y.; Song, X. M.; Gao, D. X.; Li, J. X.; Wang, Z. J.; Wang, X. Z. et al. Snail-inspired AFG/GelMA hydrogel accelerates diabetic wound healing via inflammatory cytokines suppression and macrophage polarization. *Biomaterials* **2023**, *299*, 122141.
[22] Yang, F.; Xue, Y. J.; Wang, F. L.; Guo, D. N.; He, Y. J.; Zhao, X.; Yan, F. Y.; Xu, Y. Q.; Xia, D. D.; Liu, Y. S. Sustained release of magnesium and zinc ions synergistically accelerates wound healing. *Bioact. Mater.* **2023**, *26*, 88–101.
[23] Cai, R. S.; Zhao, S.; Lu, Z. Y.; You, J. H.; Wang, H.; Xie, A. N.; Wang, S. Q.; Han, Q. Q.; Zhang, Y.; Yu, J. C. et al. Engineered thumbtack needle for augmented acupuncture therapy. *Cell Biomater.* **2025**, *1*, 100002.
[24] Chávez, J. C.; McGrath, M.; Kearney, C. J.; Browne, S.; O'Brien, F. J. Biomaterial scaffold-based gene delivery for the repair of complex wounds: Challenges, progress, and future perspectives. *Cell Biomater.* **2025**, *1*, 100073.
[25] Lyu, S.; Dong, Z. F.; Xu, X. X.; Bei, H. P.; Yuen, H. Y.; James Cheung, C. W.; Wong, M. S.; He, Y.; Zhao, X. Going below and beyond the surface: Microneedle structure, materials, drugs, fabrication, and applications for wound healing and tissue regeneration. *Bioact. Mater.* **2023**, *27*, 303–326.
[26] Zhang, X. X.; Gan, J. J.; Fan, L.; Luo, Z. Q.; Zhao, Y. J. Bioinspired adaptable indwelling microneedles for treatment of diabetic ulcers. *Adv. Mater.* **2023**, *35*, 2210903.
[27] Wang, T.; Gu, F. Y.; Xu, L. Y.; Tang, W. Q.; Han, Y. F.; Wang, Y. J.; Yang, S.; Wang, W. Y.; Zhang, X. L.; Zhao, T. S. et al. Ag nanoparticles anchored on oxygen vacancy-rich alumina catalyst for efficient bacterial inactivation. *Chem. Eng. J.* **2025**, *522*, 167731.
[28] Sisi, A.; Khataee, A.; Fathinia, M.; Vahid, B.; Orooji, Y. Comparative study of sonocatalytic process using MOF-5 and peroxydisulfate by central composite design and artificial neural network. *J. Mol. Liq.* **2020**, *316*, 113801.
[29] Biserčić, M. S.; Marjanović, B.; Vasiljević, B. N.; Mentus, S.; Zasońska, B. A.; Ćirić-Marjanović, G. The quest for optimal water quantity in the synthesis of metal-organic framework MOF-5. *Microporous Mesoporous Mater.* **2019**, *278*, 23–29.
[30] Panda, J.; Singha, D.; Panda, P. K.; Chandra Tripathy, B.; Rana, M. K. Experimental and DFT study of transition metal doping in a Zn-BDC MOF to improve electrical and visible light absorption properties. *J. Phys. Chem. C* **2022**, *126*, 12348–12360.
[31] Wu, Y. H.; Pang, H. W.; Yao, W.; Wang, X. X.; Yu, S. J.; Yu, Z. M.; Wang, X. K. Synthesis of rod-like metal-organic framework (MOF-5) nanomaterial for efficient removal of U(VI): Batch experiments and spectroscopy study. *Sci. Bull.* **2018**, *63*, 831–839.
[32] Zhang, Y.; Yang, L.; Tian, X. H.; Qiu, J. P.; Jiang, L. P.; Qiu, J. H. A water-stable two-dimensional Zn(BDC) lamellar membranes for efficient molecular separation with enhanced water permeability. *Chem. Eng. J.* **2024**, *484*, 149504.
[33] Kumar, G.; Masram, D. T. Sustainable synthesis of MOF-5@GO nanocomposites for efficient removal of rhodamine B from water. *ACS Omega* **2021**, *6*, 9587–9599.
[34] Wang, Q. Q.; Zhao, J.; Huang, T.; Sun, C.; Chen, W.; Zou, H. R.; He, X. J.; Shen, J. L.; Xiao, Y. B. Oxygen vacancy-rich nickel oxide nanoplatforms for enhanced photothermal and chemodynamic therapy combat methicillin-resistant *Staphylococcus aureus*. *Acta Biomater.* **2024**, *182*, 275–287.
[35] Liu, H. S.; Wang, X.; Wang, P.; Liu, H. T.; Wang, Q.; Xu, C. N.; Tian, H. Y. Application of metal-organic framework-based reactive oxygen species therapy in cancer. *Biomater. Sci.* **2025**, *13*, 5325–5351.
[36] He, M. M.; Wang, Z. Y.; Sun, D.; Deng, Y.; Yang, W. Z.; Yin, G. F. Type-transformational BioHJzyme enabled by composition modulation-mediated energy band engineering for diabetic infectious wound healing. *Adv. Funct. Mater.* **2025**, *35*, 2421228.
[37] Wen, S. W.; Zhang, W. Y.; Yang, J. L.; Zhou, Z. J.; Xiang, Q.; Dong, H. F. Ternary $Bi_2WO_6$/$TiO_2$–Pt heterojunction sonosensitizers for boosting sonodynamic therapy. *ACS Nano* **2024**, *18*, 23672–23683.
[38] Yadav, D.; Malviya, R. Novel nanomaterials as photo-activated cancer diagnostics and therapy. *Med. Adv.* **2023**, *1*, 190–209.
[39] Chen, S. Q.; Shao, A.; Xia, C.; Zeng, L. T.; Sun, Z. J.; Zhu, J. Y.; Ding, W. J.; Yang, Q. N.; Yu, B.; He, Q. J. Local sustained $H_2$ release assisted stem cell transplantation for enhanced osteoarthritic cartilage regeneration. *Cell Biomater.* **2025**, 100220.
[40] Wang, M. J.; Song, X. J.; Liu, X. L.; Ma, C.; Ma, J.; Shi, L. L. Engineered oncolytic bacteria for malignant solid tumor treatment. *Interd. Med.* **2024**, *2*, e20240005.
[41] Cui, Y.; Niu, Q.; Hu, Z. Y.; He, H.; Wei, X. L.; Wang, M.; Chen, X. L.; Wang, X. W. Multifunctional nanozyme-hydrogel system in bacterial-infected wounds. *Cell Biomaterials,* **2025**, *1*, 100074.
[42] Zhao, Y. N.; Tian, C.; Liu, Y. M.; Liu, Z. Q.; Li, J.; Wang, Z. J.; Han, X. W. All-in-one bioactive properties of photothermal nanofibers for accelerating diabetic wound healing. *Biomaterials* **2023**, *295*, 122029.
[43] Mateu-Sanz, M.; Fuenteslópez, C. V.; Uribe-Gomez, J.; Haugen, H. J.; Pandit, A.; Ginebra, M. P.; Hakimi, O.; Krallinger, M.; Samara, A. Redefining biomaterial biocompatibility: Challenges for artificial intelligence and text mining. *Trends Biotechnol.* **2024**, *42*, 402–417.
[44] Bochenek, M.; Mendrek, B.; Kowalczuk, A.; Wałach, W.; Jałowiecki, L.; Borgulat, J.; Płaza, G.; Kubacki, J.; Sikora, M.; Fus-Kujawa, A. et al. Designing antibacterial polymeric systems: (Co)poly(2-oxazoline) conjugates with acyclic and macrocyclic polyamino polycarboxylic chelators. *Biomater. Sci.* **2025**, *13*, 3876–3886.
[45] Piao, Y.; Himbert, S.; Li, Z. F.; Liu, J.; Zhao, Z. H.; Yu, H. H.; Liu, S. S.; Shao, S. Q.; Fefer, M.; Rheinstädter, M. C. et al. Alkylated EDTA potentiates antibacterial photodynamic activity of protoporphyrin. *J. Nanobiotechnol.* **2024**, *22*, 161.
[46] Wang, W. Q.; Gui, H. S.; Wei, X. L.; Liu, H. Y.; Wang, X. W. Cuproptosis to cuproptosis-like: Therapeutic strategies for bacterial infection. *Adv. Mater.* **2025**, *37*, 2506119.
[47] Arunkumar, T.; Castelino, E.; Lakshmi, T.; Mulky, L.; Selvanathan, S. P.; Tahir, M. Metal-organic frameworks in antibacterial disinfection: A review. *ChemBioEng Rev.* **2024**, *11*, e202400006.
[48] Doan, T. D.; Vu, N. N.; Hoang, T. L. G.; Nguyen-Tri, P. Metal-organic framework (MOF)-based materials for photocatalytic antibacterial applications. *Coord. Chem. Rev.* **2025**, *523*, 216298.
[49] Feng, X.; Luo, Z. W.; Zhang, W.; Wan, R. W.; Chen, Y. S.; Li, F. Q.; He, Y. W.; Lin, Z. H.; Hui, J. H.; Conde, J.; et al. Zn-DHM nanozymes enhance muscle regeneration through ROS scavenging and macrophage polarization in volumetric muscle loss revealed by single-cell profiling. *Adv. Funct. Mater.* **2025**, *35*, 2506476
[50] Yang, C.; Lian, H.; Luo, H. L.; Song, C. L.; Lin, J. H.; Liang, Z. X.; Yang, Y. L.; Hong, X. S.; Li, S. H.; Chen, Y. B. et al. The diminution of R-loops generated by LncRNA DSP-AS1 inhibits DSP gene transcription to impede the Re-epithelialization during diabetic wound healing. *Adv. Sci.* **2025**, *12*, e2406021.
[51] Cui, F. H.; Fu, W. J.; Chang, Q.; Wang, J.; Xie, Y. J.; Deng, X. Y. ROS-modulating bio-heterojunction nanosheets for infected wound healing via nanozyme activity. *Small* **2025**, *21*, 2412441.
[52] Li, Y. F.; Du, K. Y.; Peng, D. F.; Zhang, X. L.; Piao, Y. Z.; Peng, M. N.; He, W.; Wang, Y. M.; Wu, H. Y.; Liu, Y. et al. Local delivery of siRNA using lipid-based nanocarriers with ROS-scavenging ability for accelerated chronic wound healing in diabetes. *Biomaterials* **2025**, *322*, 123411.
[53] Zhao, Y. S.; Zhao, S. Q.; Du, Y.; Gao, Z. F.; Li, Y. L.; Ma, H. M.; Li, H.; Ren, X.; Fan, Q.; Wu, D. et al. Inverse oxide/alloy-structured nanozymes with NIR-triggered enzymatic cascade regulation of ROS homeostasis for efficient wound healing. *Adv. Mater.* **2025**, *37*, 2418731.
[54] Zhang, J. Y.; Zhao, S. F.; Zhou, Y. F.; Liang, H. Z.; Zhao, L. L.; Tan,

H. Carboxymethyl chitosan-based antioxidant hydrogel accelerates diabetic wound healing. *Adv. Healthc. Mater.* **2025**, *14*, 2403198.

[55] Zhou, X.; Yu, X. Z.; You, T. T.; Zhao, B. H.; Dong, L. L.; Huang, C.; Zhou, X. Q.; Xing, M.; Qian, W.; Luo, G. X. 3D printing-based hydrogel dressings for wound healing. *Adv. Sci.* **2024**, *11*, e2404580.

[56] Zhu, Z. Y.; Zhou, S. Z.; Li, S. C.; Gong, S.; Zhang, Q. Neutrophil extracellular traps in wound healing. *Trends Pharmacol. Sci.* **2024**, *45*, 1033–1045.

[57] Yang, Y. Y.; Zhong, S. L.; Meng, F. Y.; Cui, X. J. Multi-functional hydrogels to promote diabetic wound healing: A review. *Chem. Eng. J.* **2024**, *497*, 154855.

[58] Yan, L. F.; Wang, J.; Cai, X.; Liou, Y. C.; Shen, H. M.; Hao, J. L.; Huang, C. H.; Luo, G. X.; He, W. F. Macrophage plasticity: Signaling pathways, tissue repair, and regeneration. *MedComm* **2024**, *5*, e658.

[59] Peña, O. A.; Martin, P. Cellular and molecular mechanisms of skin wound healing. *Nat. Rev. Mol. Cell Biol.* **2024**, *25*, 599–616.

[60] Zhang, Z. H.; Xue, H.; Xiong, Y.; Geng, Y. T.; Panayi, A. C.; Knoedler, S.; Dai, G. D.; Shahbazi, M. A.; Mi, B. B.; Liu, G. H. Copper incorporated biomaterial-based technologies for multifunctional wound repair. *Theranostics* **2024**, *14*, 547–570.

[61] Li, L. S.; Sun, Y. A.; He, H. H.; He, G. Y.; Ma, S. H.; Yang, W. F.; Wang, Y. Quantitative assessment of angiogenesis in skin wound healing by multi-optical imaging techniques. *Front. Phys.* **2022**, *10*, 2022.

[62] Chen, Z. S.; Zhang, Y. X.; Feng, K. X.; Hu, T.; Huang, B. H.; Tang, J. L.; Ai, J. J.; Guo, L.; Hu, W. K.; Wang, Z. J. Facile fabrication of quaternized chitosan-incorporated biomolecular patches for non-compressive haemostasis and wound healing. *Fundam. Res.* **2024**, *4*, 1243–1253.

[63] Luo, J. T.; Song, T.; Han, T. T.; Qi, H. S.; Liu, Q. H.; Wang, Q.; Song, Z. Q.; Rojas, O. Multifunctioning of carboxylic-cellulose nanocrystals on the reinforcement of compressive strength and conductivity for acrylic-based hydrogel. *Carbohydr. Polym.* **2024**, *327*, 121685.

[64] Haghniaz, R.; Rabbani, A.; Vajhadin, F.; Khan, T.; Kousar, R.; Khan, A. R.; Montazerian, H.; Iqbal, J.; Libanori, A.; Kim, H. J. et al. Anti-bacterial and wound healing-promoting effects of zinc ferrite nanoparticles. *J. Nanobiotechnology* **2021**, *19*, 38.

[65] Wang, X.; He, X. H.; Liu, X. Y.; Chen, M. J.; Wang, Y. H.; Guo, C. Q.; Wang, J. P.; Zhang, H.; Hao, Y. C.; Wei, Y. et al. Near-infrared light-triggered smart response platform integrating $CeO_2$@Black phosphorus for enhanced antimicrobial, anti-inflammatory, and osseointegration properties of titanium implants. *Compos. Part B: Eng.* **2025**, *291*, 112044.